REMMA

Research in ElectroMagnetic
Medical Applications

BOOK OF ABSTRACTS

1st Student Conference
Research in ElectroMagnetic Medical Applications
Zelezna Ruda, Czech Republic
12-15 September 2023

Conference Committee

prof. Dr.-Ing. Jan Vrba, M.Sc., Chairman of the Organizing Committee

Email: jan.vrba@fbmi.cvut.cz

doc. Ing. David Vrba, Ph.D., Vice-Chairman of the Organising Committee

Email: david.vrba@fbmi.cvut.cz

Ing. Tomas Pokorny, Ph.D., Main organizer of the REMMA 2023 conference

Email: jan.vrba@fbmi.cvut.cz

Ing. Tomas Drizdal, Ph.D., Chairman of the Diagnostics Section

Email: tomas.drizdal@fbmi.cvut.cz

doc. Ing. Ondrej Fiser, Ph.D., Chairman of the Therapy Section

Email: ondrej.fiser@fbmi.cvut.cz

Ing. Marek Novak, Ph.D., Expert speech and presentation

Email: marek.novak@cvut.cz

Editor of the proceedings: Tomas Pokorny

Published in September 2023

The proceedings are available in electronic form at bioem.fbmi.cvut.cz

Acknowledgements

The REMMA conference was supported by the CTU in Prague, project number SVK 58/23/F7 of the Student Grant Competition of the CTU in Prague.


REMMA
STUDENT CONFERENCE
Research in Electromagnetic
Medical Applications
Czech Technical University in Prague
Faculty of Biomedical Engineering


REMMA
REMMA
Certificate
REMMA
Certificate
REMMA
Certificate

Numerical feasibility study of UWB radar monitoring of RF Numerical feasibility study of UWB radar monitoring of RF liver ablation

J. Kollar, O. Fiser

Department of Biomedical Technology, Faculty of Biomedical Engineering,
Czech Technical University in Prague, Kladno, Czech Republic

Abstract: Liver cancer is one of the most common tumor diseases worldwide. Radiofrequency (RF) thermal ablation of hepatocellular carcinomas is an essential treatment modality. The continuous monitoring of RF ablation is crucial for the treatment efficiency and patient safety. One of the promising methods for continuous monitoring of RF treatment is microwave imaging [1]. The main objective of this study was a numerical investigation of RF liver ablation monitoring using UWB radar. The ablation monitoring via UWB radar is a differential imaging method based on the reflections caused by a contrast in the dielectric properties of an ablated region. During the RF ablation procedure, the dielectric properties of the tissue decrease significantly when the temperature increases above 60 °C [2].

Simulation of the torso of an anthropomorphic heterogenous human model from the Virtual Family (specifically Duke model) was implemented in Sim4Life and the dielectric properties were assigned from IT'IS foundation database [3]. The eight UWB bowtie antennas were adopted from [4] and uniformly distributed around the liver area. The antennas were excited by the Gaussian pulse with frequencies ranging from 1 to 6 GHz. The catheter model (with diameter of 2 mm) was placed into the tumor position within the liver. The three concentric ellipsoids-shaped ablation zones were placed around the catheter to simulate the real clinical situation. Changes in the dielectric parameters caused by the ablation were taken from [2]. From the recorded signals the clutter was subtracted and results were visualized using the “Delay and Sum” algorithm. We considered three tumor positions in total. The resulting image reconstructions captured the interface of ablated and intact tissue. Thus, a methodology for determining the accuracy of ablated zone boundary detection was created.

This numerical analysis demonstrates the potential of the method to continuously monitor the ablation process using UWB radar. The ablation zones of three tumor positions were successfully reconstructed with a mean accuracy lower than 2 mm. The results suggest that the UWB radar monitoring is applicable for continuous RF ablation monitoring with accuracy that is sufficient for therapeutic purposes.

REFERENCES

[1] M. Wang, R. Scapaticci, M. Cavagnaro, and L. Crocco, “Towards a Microwave Imaging System for Continuous Monitoring of Liver Tumor Ablation: Design and In Silico Validation of an Experimental Setup,” Diagnostics, vol. 11, no. 5, p. 866, May 2021, doi: 10.3390/diagnostics11050866.

[2] V. Lopresto, R. Pinto, G. A. Lovisolo, and M. Cavagnaro, “Changes in the dielectric properties of ex vivo bovine liver during microwave thermal ablation at 2.45 GHz,” Phys Med Biol, vol. 57, no. 8, p. 2309, Mar. 2012, doi: 10.1088/0031-9155/57/8/2309.

[3] P. Hasgall and E. Neufeld, “IT’IS database for thermal and electromagnetic parameters of biological tissues.” 2017, Accessed: Jan. 10, 2023. [Online]. Available: www.itis.ethz.ch/database.

[4] O. Fiser et al., "UWB Bowtie Antenna for Medical Microwave Imaging Applications," in IEEE Transactions on Antennas and Propagation, vol. 70, no. 7, pp. 5357-5372, July 2022, doi: 10.1109/TAP.2022.3161355.

Comparison of Materialise Mimics and 3D Slicer segmentation softwares for creating anatomical 3D models

Barbora Jirásková

Department of Biomedical Technology, Faculty of Biomedical Engineering,
Czech Technical University in Prague, Kladno, Czech Republic

Introduction: Hyperthermia treatment is usually combined with standard chemotherapy, radiotherapy or immunotherapy for treatments of various cancer diseases [1]. The outcome hyperthermia treatment strongly depends at the temperature achieved in the tumor region [2]. For tumors in the abdomen and pelvic region a constructive interference of several electromagnetic waves radiated from the antenna elements surrounding the patient is used. Amplitude and phases of antenna input signals are optimized using virtual 3D patient specific model and the model of the phased array system in order to maximize the heat delivery in the target region. In this hyperthermia treatment planning process, it is essential to create patient 3D models that take into account the individual characteristics of each patient.

The aim of this project was to compare two segmentation software for generating 3D anatomical models based on medical CT images.

Methods: Both *Materialise Mimics 22.0* and *3D Slicer 5.2.2* were compered in terms of creating 3D patient models. Models were created using freely available medical CT scans. Both programs utilize thresholding allowing semiautomatic segmentation of bones, fat, muscle, lung, and internal air. Further both programs allow manual corrections and delineations of individual organs or the region of interest for optimization. The program *Materialise* allows for the automated segmentation of an adult patient's various anatomical tissues including skin, muscle, fat, bones and air. On the other hand, *3D Slicer* contains a Total Segmentation toolbox for artificial intelligence (AI) automated segmentation of up to 104 organs in the body except for fat tissue. Materialise launches an automatic segmentation tool enabled by AI, however, it will be a new paid license. The 3D patient models are further exported to electromagnetic field simulators, COMSOL Multiphysics and Sim4Life.

Results: The resulting 3D models show significant differences. Using automated segmentation in the *3D Slicer* program allows for precise delineation of patient segments within a matter of minutes. However, these automated organs delineations need to be accompany threshold segmentation of adipose and muscle tissues in the model which are essential for therapeutic hyperthermia treatment planning. On the other hand, in the Materialise program, it is not possible to achieve the same level of detailed segmentation as with *3D Slicer*.

Conclusion: In this study, *3D Slicer* appears to be the more advantageous and straightforward program for segmenting patient images for hyperthermia treatment planning purpose including scenarios where detailed segmentation is required. The choice of segmentation tool also depends on the intended use of these models. Segmentation of 104 tissues in *3D Slicer* is as time consuming as segmentation of 5 tissues in *Materialise*. In addition, the *3D Slicer* is a free, open-source software, whereas *Materialise* has paid license.

REFERENCES

[1] Proven Clinical Evidence: Hyperthermia improves Clinical Outcome. *Pynexar MEDICAL* [online]. Salt lake City, 2004 [cit. 2023-04-16]. Dostupné z: https://www.pyrexar.com/clinical

[2] PAULIDES, Margarethus M., Dario B. RODRIGUES, Gennaro G. BELLIZZI, et al. ESHO benchmarks for computational modeling and optimization in hyperthermia therapy. International Journal of Hyperthermia [online]. 2021, 38(1), 1425-1442 [cit. 2023-04-16]. ISSN 0265-6736. Dostupné z: doi:10.1080/02656736.2021.1979254

Optimization strategies for hyperthermia treatment

Michaela Cerna[1], Tomas Drizdal[1]

Department of Biomedical Technology, Faculty of Biomedical Engineering,
Czech Technical University in Prague, Kladno, Czech Republic

Microwave hyperthermia is a therapeutic technique using electromagnetic waves to elevate temperatures in neoplastic tissue between 40 and 44 °C. It disrupts essential cellular processes within cancerous cells, eventually leading to their demise. This method is commonly used with radiotherapy as it impairs DNA repair mechanisms in tumor cells [1]. Moreover, when combined with chemotherapy, hyperthermia has shown promising results by enhancing drug accumulation within the affected areas of tumors and improving overall drug efficacy [2]. Nevertheless, one significant challenge during hyperthermia treatment is the precise delivery of heat exclusively to the tumor region while minimizing adverse effects on surrounding healthy tissues. For deep seated targets a constructive interference of several electromagnetic waves radiated for antenna elements within the phased array system are used. Antennas are submerged in deionized water representing the water bolus used to cool the surface regions.

The effectiveness of hyperthermia treatment can be evaluated using a parameter called Specific Absorption Rate (SAR). However, SAR cannot be directly measured during the treatment process. To overcome this limitation, treatment planning techniques are employed. These techniques typically involve three key steps: segmentation, electromagnetic simulation, and phase and amplitude optimization of antenna input signals [3]. During the phase and amplitude optimization step, two main approaches can be used: SAR-based optimization and temperature-based optimization. With SAR-based optimization, the goal is on finding the optimal phase and amplitude settings for the antenna elements with respect to maximize the computational speed and efficiency. On the other hand, temperature-based optimizations involve solving the bioheat equation at each iteration step which leads to slower computation speeds but may provide alternative advantages, such as incorporating cooling mechanism of the body to the tumor region while minimizing adverse effects on surrounding healthy tissues.

This study investigates a comparison of four SAR-based optimization algorithms. The algorithms under investigation included three iterative approaches, namely Surrogate Optimization (SGO) [4], Particle Swarm Optimization (PSO) [5], and Genetic Algorithm (GA) [6]. Additionally, a non-iterative method called Time Reversal Focusing (TRF) was also

considered [7]. To evaluate the performance of these algorithms, two functions were employed: the Target Hotspot Quotient function (THQ) and the Target Convergence function (TC). THQ provides a ratio of the relationship between the average SAR within tumors and an average SAR in 1 % of the healthy tissue with the highest value. TC parameter quantifies the extent to which the target hyperthermia volume is encompassed by an iso-SAR that meets or exceeds a certain threshold, denoted as x %. In clinical practice, TC25 is employed as a determining factor for assessing the feasibility of hyperthermia treatment. Treatment is deemed viable if TC25 exceeds 75 %.

In this study, various software programs were used. Specifically, the iSeg program was employed to generate three-dimensional patient models. For glioblastoma patients with available MRI images, the initial step involved registering both CT and MRI images. This registration process was carried out in Matlab using the SPM12 toolbox. Electromagnetic simulations were conducted using Sim4Life, while the actual optimizations were done within Matlab.

Our findings revealed that the PSO algorithm, which is commonly used in clinical settings, demonstrated favorable outcomes for tumors located in the head and neck area. However, when it came to brain tumors, both the GA and SGO algorithms exhibited better performance than PSO Since comparable results were obtained from these two algorithms, their comparison was further examined based on their ability to produce consistent results. Consequently, it was observed that the SGO algorithm demonstrated higher reproducibility and thus offered greater stability in identifying global minima.

REFERENCES

[1] KOK, HP, P. WUST, PR STAUFFER, F BARDATI, GC VAN RHOON a J. CREZEE. Current state of the art of regional hyperthermia treatment planning: a review. *Radiation Oncology*. 2015, **10**(1). ISSN 1748-717X. Dostupné z: doi:10.1186/s13014-015-0503-8

[2] CHEN, Zhanying, Xuekun LI, Zongyu ZHU, Zeming ZHAO, Liping WANG, Sheng JIANG a Yiming RONG. The optimization of accuracy and efficiency for multistage precision grinding process with an improved particle swarm optimization algorithm. *International Journal of Advanced Robotic Systems*. 2020, **17**(1). ISSN 1729-8814. Dostupné z: doi:10.1177/1729881419893508

[3] GAVAZZI, Soraya, Astrid L. H. M. W. VAN LIER, Cornel ZACHIU, Eric JANSEN, Jan J. W LAGENDIJK, Lukas J. A STALPERS, Hans CREZEE a H. Petra KOK. Advanced patientspecific hyperthermia treatment planning. *International Journal of Hyperthermia*. 2020, **37**(1), 992-1007. ISSN 0265-6736. Dostupné z: doi:10.1080/02656736.2020.1806361

[4] QUEIPO, Nestor V., Raphael T. HAFTKA, Wei SHYY, Tushar GOEL, Rajkumar VAIDYANATHAN a P. KEVIN TUCKER. Surrogate-based analysis and optimization.

Progress in Aerospace Sciences. 2005, **41**(1), 1-28. ISSN 03760421. Dostupné z: doi:10.1016/j.paerosci.2005.02.001

[5] ROBINSON, J. a Y. RAHMAT-SAMII. Particle swarm optimization in electromagnetics. *IEEE Transactions on Antennas and Propagation*. 2004, **52**(2), 397-407. ISSN 0018-926X. Dostupné z: doi:10.1109/TAP.2004.823969

[6] ALDHAEEBI, Maged, Mohammad ALZABIDI a Ibrahim ELSHAFIEY. Genetic Algorithm Optimization of SAR Distribution in Hyperthermia Treatment of Human Head. *2013 1st International Conference on Artificial Intelligence, Modelling and Simulation*. IEEE, 2013, 92-97. ISBN 978-1-4799-3251-1. Dostupné z: doi:10.1109/AIMS.2013.22

[7] TREFNÁ, Hana Dobšíček, Jan VRBA a Mikael PERSSON. Time-reversal focusing in microwave hyperthermia for deep-seated tumors. *Physics in Medicine and Biology*. 2010, **55**(8), 2167-2185. ISSN 0031-9155. Dostupné z: doi:10.1088/0031-9155/55/8/004

System for regional hyperthermia treatment in the head and neck region

Matěj Mácha

Department of Biomedical Technology, Faculty of Biomedical Engineering,
Czech Technical University in Prague, Kladno, Czech Republic

1. INTRODUCTION

Hyperthermia is a way of enhancing the effectivity of direct cancer therapy methods like radiotherapy and chemotherapy, but without increasing its possible toxicity. The effect is based on inhibition of DNA repair and aggregation of protein in the cell nuclei of the target tissue [1, 2, 3]. Hyperthermia can be applied in several ways, including using an electromagnetic field [4]. Many hyperthermia systems that use an electromagnetic field have been designed, one of which is the clinically applied HYPERCollar system [1]. The goal of this research is to design a system for regional hyperthermia treatment in the head and neck region.

2. METHODS

A hyperthermia treatment system was designed in the Sim4Life (V 7.0.0.7995) program, consisting of a waterbolus surrounded by a plexiglass frame with 12 Yagi-Uda antennas, optimized for the frequency of 434 MHz [5], a standard frequency for surface hyperthermia treatment in Europe. Antennas were placed on the sides of the frame, as seen in figure 2.1.

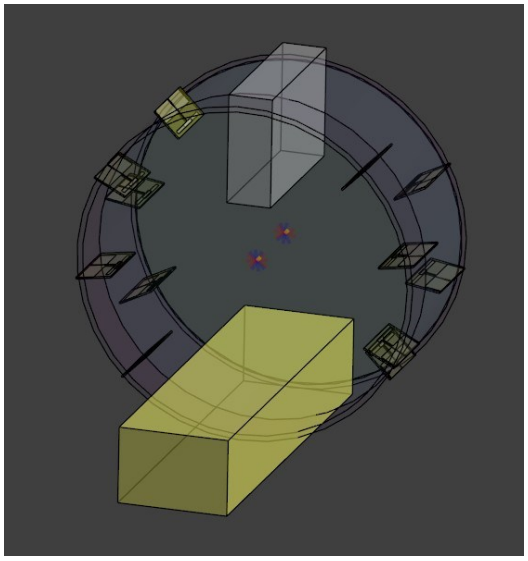

Figure 2.1: An overview of the designed hyperthermia treatment system

To test and optimize the system, three-dimensional patient models with tumors in the head and neck region were created – three with a tumor in the head area and three with a tumor in the neck area. Using the iSEG (v3.10.57.98) program, publicly accessible and anonymized CT and MRI images were segmented and imported into Sim4Life. Simulations were done

with the aim of achieving a maximum of 44 °C in healthy tissue. To this end, total power of 250 W was distributed among the antennas. Dielectric parameters form the IT'IS Foundation database were used in the simulations, with a discretization step of 1 second and a total thermal simulation time of 1 hour. Sim4Life function *HyperTOptimizer* was set to maximize SAR in the target tumor area and minimize it in eye tissues.

3. RESULTS

Resulting SAR coverage of the target area and its temperature were captured in slices in the middle of the tumor. The SAR and temperature of one of the models used is shown in figures 3.1 and 3.2. The tumor, red and half-opaque is visible on the right side of the brain. The scale for SAR has a maximum of 50 W and minimum of 0 W, whereas the temperature scale ranges from 36 °C to 44 °C. The color scale is shown in the top left corner.

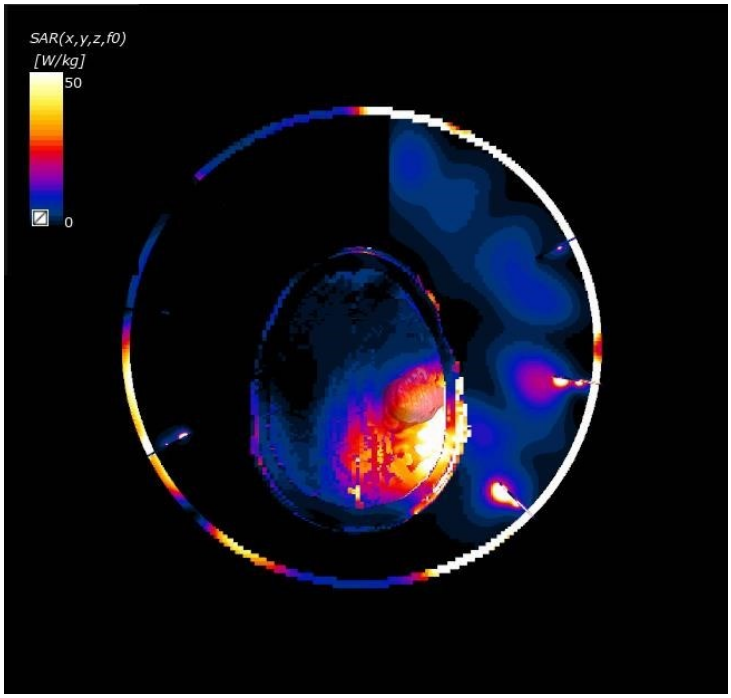

Figure 3.1: SAR coverage of the target area

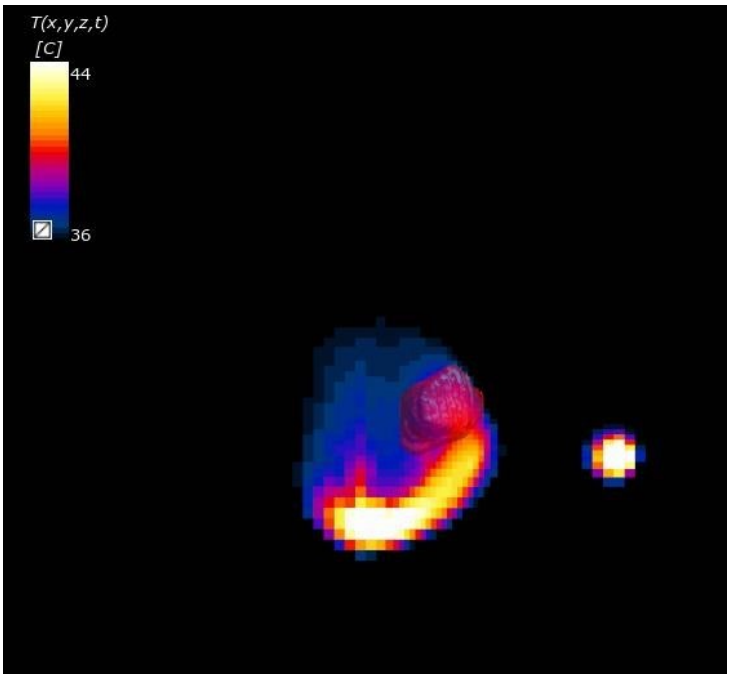

Figure 3.2: Temperature in the target area

4. DISCUSSION AND CONCLUSION

A system for hyperthermia treatment in the head and neck region was designed in the Sim4Life program. Electromagnetic and thermal simulations were carried out for six different patient models with the aim of achieving no more than 44 °C in the model. The results of the simulations depended heavily on the patient model used. The target areas of the second head tumor and the third neck tumor model were well covered with SAR and heated, whereas the first and third head tumor model and the first neck tumor model had inadequate heating depth. The second neck tumor model could not be heated because of the tumor placement, which turned out to be too low in the neck – consequentially, the system could not be properly placed.

Additional adjustments to the system design might be necessary before its construction.

REFERENCES

[1] VERDUIJN, G. M., E. M. DE WEE, Z. RIJNEN, et al. Deep hyperthermia with the HYPERcollar system combined with irradiation for advanced head and neck carcinoma – a feasibility study. *International Journal of Hyperthermia* [online]. 2018, **34**(7), 994-1001 [cit. 2023-06-17]. ISSN 0265-6736. Dostupné z: doi:10.1080/02656736.2018.1454610

[2] OEI, Arlene L., Lianne E. M. VRIEND, Johannes CREZEE, Nicolaas A. P. FRANKEN a Przemek M. KRAWCZYK. Effects of hyperthermia on DNA repair pathways: one

treatment to inhibit them all. *Radiation Oncology* [online]. 2015, **10**(1) [cit. 2023-06-18]. ISSN 1748-717X. Dostupné z: doi:10.1186/s13014-015-0462-0

[3] KAMPINGA, Harm H. Cell biological effects of hyperthermia alone or combined with radiation or drugs: A short introduction to newcomers in the field. *International Journal of Hyperthermia* [online]. 2009, **22**(3), 191-196 [cit. 2023-04-24]. ISSN 0265-6736. Dostupné z: doi:10.1080/02656730500532028

[4] KOK, H. Petra, Erik N. K. CRESSMAN, Wim CEELEN, et al. Heating technology for malignant tumors: a review. *International Journal of Hyperthermia* [online]. 2020, **37**(1), 711-741 [cit. 2023-06-20]. ISSN 0265-6736. Dostupné z: doi:10.1080/02656736.2020.1779357

[5] DRIZDAL, Tomas, Kemal SUMSER, Gennaro G. BELLIZZI, Ondrej FISER, Jan VRBA, Gerard C. van RHOON, Desmond T. B. YEO a Margarethus M. PAULIDES. Simulation guided design of the MRcollar: a MR compatible applicator for deep heating in the head and neck region. *International Journal of Hyperthermia* [online]. 2021, **38**(1), 382-392 [cit. 2023-06-23]. ISSN 0265-6736. Dostupné z: doi:10.1080/02656736.2021.1892836

Design of a system for distance measurement inside a water bolus during microwave regional hyperthermia treatment

D. Janoušek[1], Ing. M. Novák, Ph.D.[1] and T Dřížďal, Ph.D.[1]

Department of Biomedical Technology, Faculty of Biomedical Engineering,
Czech Technical University in Prague, Kladno, Czech Republic

Abstract—In this article a system for underwater distance measurement for microwave regional hyperthermia treatment is proposed and tested. For this purpose, many distance measurement technologies were researched and compared. The properties and behavior of chosen sensors were experimentally tested. The criteria for desired sensor were distance measurement between 0 and 150 mm with accuracy at least ±5 mm. Sensor measured distance was compared to manual distance measurement and statistically evaluated. The chosen sensor VL53L1X is optical sensor which measured in desired range with standard deviation ±1.22 mm.

1. INTRODUCTION

The hyperthermic systems are one of the latest approaches for cancer treatment. For this treatment to be effective, produced microwaves must be focused on the cancer tumor. Additionally, a more focused microwave system limits microwave energy radiation to healthy tissue. This focusing of hyperthermic system could even shorten a therapy duration.

Every patient is of different shape, size, breaths in different frequency and position itself in the hyperthermic chamber differently. All these factors influence the accuracy thus effectivity of hyperthermic treatment.

Different distance measurement methods were researched. One of the most used methods is use of ultrasonic time of flight sensors. These sensors are temperature dependent because of change in density of the medium in which the sound waves travel [1]. The ultrasonic sensors also have a dead zone where the sensor cannot measure [2]. In water this dead zone is prolonged as the sound travels faster in water than in air. This means that most of ultrasonic sensors are unusable for our application where we need to measure in short distances. With the use of multiple sensors there is a higher risk of interference between the sensors.

Other used method is optical. Optical sensors use the same time of flight principle as ultrasonic but instead of mechanical waves they use light. The light doesn't need medium to propagate and so is much less dependent on it. The speed of light dwarfs the effects of temperature and density on the accuracy [3, 4]. What isn't negligible is the absorbance of sensed object and the medium the light travels through. The effect of absorbance of the object could be lowered by choosing suitable color for the membrane which separates patient from the water bolus. The optical sensors suffer from crosstalk which is an artifact which occurs when the light travels through materials with different refractive index. This makes some portions of the light to scatter and reflect to the sensor faster than the light reflected from measured object [5]. This effect can be compensated in some sensors. The optical time of flight sensors have potential to be very accurate.

Inductive and camera systems were also explored. These systems tend to be very artifact sensitive, spacious, or expensive [6, 7].

2. METHODS

For the experimental measurement sensors JSN-SR04T, HY-SRF05, VL53L0X and VL53L1X were used. For sonic sensors JSN-SR04T and HY-SRF05 an Arduino script was created.

For optical sensors VL53L0X and VL53L1X an Arduino script was created with the use of STMicroelectronics library [8].

The sensors were isolated from the water with the use of duct tape. The waterproofed sensor was submerged, and crosstalk calibrated in distance where crosstalk artifact started.

The measurement was conducted in transparent plastic container filled with tempered water in room temperature with the access of ambient light. The target was gray plate of plastic. Sensor was fixed on one side and the target was moving from the sensor in incremental steps of 30 mm to the distance of 150 mm. The data gained from this measurement was processed and statistics were made.

3. RESULTS

The averages of sensor measured distances were plotted in the graph 1 with the ideal measurements. The ideal measurements equal to the real distance.

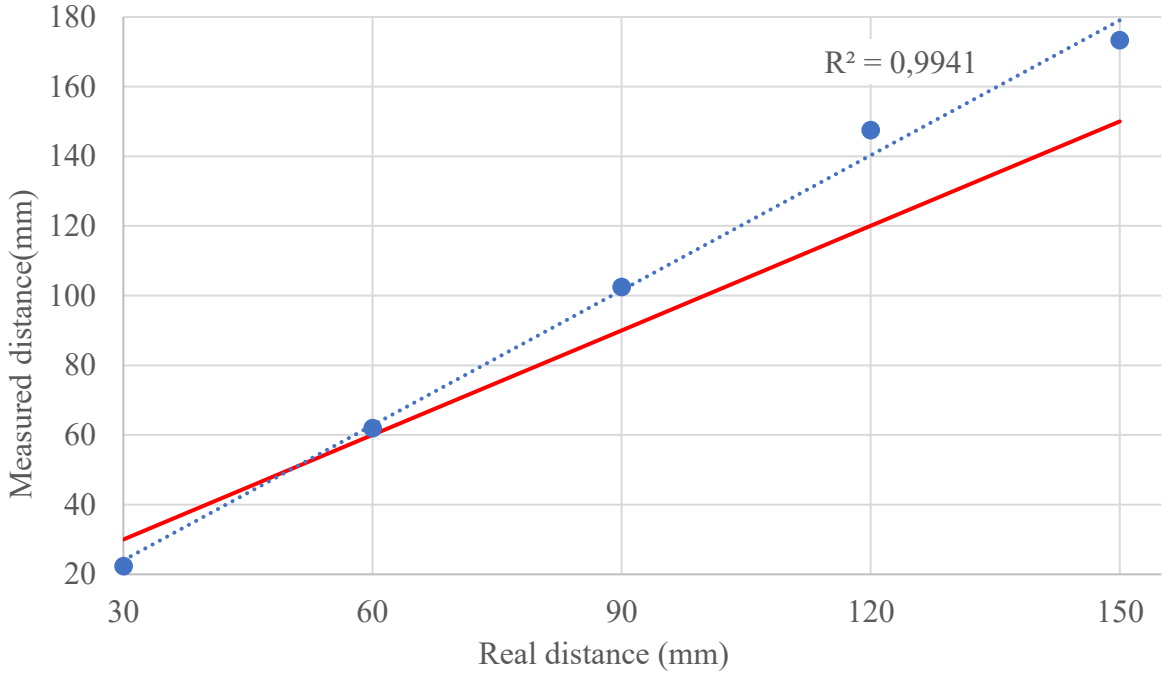

Figure 1: The difference between distance measured and real. The VL53L1X sensor measured data are plotted in blue dotted line, while the ideal distance measurements are plotted in full red line.

The results of statistics for every distance measured are in table 1.

Table 1: VL53L1X sensor statistics for underwater measurement.

Real distance (mm)	**30**	**60**	**90**	**120**	**150**
Mean (mm)	22	62	102	148	173
Standard deviation (mm)	±0,73	±0,83	±1,22	±0,73	±0,88
Absolute interval (mm)	3	2	4	3	3

4. DISCUSSION

The VL53L1X sensor successfully measures distance in range to 150 mm with maximum standard deviation of ±1,22 mm from its linear regression. The data measured visibly follow linear trend with 99,41 % accuracy. This is important because this means that the deviation from ideal could be easily compensated.

In the following design more accurate color for crosstalk calibration will be used which should ensure even higher linearity of measured data.

During the experimenting it was found out that the VL53L0X is very comparable to the VL53L1X but doesn't allow measurement in the desired range.

The ultrasonic sensors JSN-SR04T and HY-SRF05 showed as inapplicable. When submerged these sensors showed constant value and didn't respond to any target movement. There was no further experimenting done with these sensors.

5. CONCLUSION

The sensor VL53L1X has proven effective in underwater distance measurement in the range of 0–150 mm with small standard deviation of ±1,22 mm.

REFERENCES

[1] WAN, Dennis Zhen a Cheng Siong CHIN. Simulation and prototype testing of a low-cost ultrasonic distance measurement device in underwater. *Journal of Marine Science and Technology* [online]. 2015, **20**(1), 142-154 [cit. 2023-06-11]. ISSN 0948-4280. Source: doi:10.1007/s00773-014-0270-5

[2] *RBR: All about speed of sound in water – what it is, how it's measured, and why we care* [online]. RBR, 2023 [cit. 2023-06-11]. Source: https://rbr-global.com/speed-of-sound-in-water/

[3] *University of Toronto Scarborough: Refractive Index Theory* [online]. 1265 Military Trail, Toronto, ON. Canada: UTSCUniversity of Toronto Scarborough [cit. 2023-06-11]. Source: https://www.utsc.utoronto.ca/webapps/chemistryonline/production/refractive.php

[4] ADRIÁN-MARTÍNEZ, S., I. AL SAMARAI, A. ALBERT, et al. *Astroparticle Physics* [online]. 2012, **35**(9) [cit. 2023-06-11]. ISSN 09276505. Source: doi:10.1016/j.astropartphys.2011.12.003

[5] BORENSTEIN, J. a Y. KOREN. Error eliminating rapid ultrasonic firing for mobile robot obstacle avoidance. *IEEE Transactions on Robotics and Automation* [online]. **11**(1), 132-138 [cit. 2023-06-11]. ISSN 1042296X. Source: doi:10.1109/70.345945

[6] AKYILDIZ, Ian F., Pu WANG a Zhi SUN. Realizing underwater communication through magnetic induction. *IEEE Communications Magazine* [online]. 2015, **53**(11), 42-48 [cit. 2023-06-11]. ISSN 0163-6804. Source: doi:10.1109/MCOM.2015.7321970

[7] MASSOT-CAMPOS, Miquel a Gabriel OLIVER-CODINA. Optical Sensors and Methods for Underwater 3D Reconstruction. *Sensors* [online]. 2015, **15**(12), 31525-31557 [cit. 2023-06-11]. ISSN 1424-8220. Source: doi:10.3390/s151229864

[8] *GitHub: X-NUCLEO-53L1A1* [online]. GitHub, 2023 [cit. 2023-06-11]. Source: https://github.com/stm32duino/X-NUCLEO-53L1A1

Design of a catheter for microwave ablation of pancreatic tumors

Dominik Cizek

Department of Biomedical Technology, Faculty of Biomedical Engineering,
Czech Technical University in Prague, Kladno, Czech Republic

1. INTRODUCTION

The pancreas is a pear-shaped glandular organ about the size of a human palm, located in the abdominal cavity between the stomach and the spine. This deep location of the pancreas in the abdominal cavity causes any disease, including pancreatic cancer, to have no symptoms for a long time and to be diagnosed only in advanced stages. For this reason, the 5-year relative survival rate for pancreatic tumors is only 12% (USA) [1]. However, this is a combined statistic for exocrine and endocrine (PNET) tumors combined. The 5-year survival rate for exocrine tumors alone is 5.0% and 51.3% for PNETs [2].

The most common treatment for pancreatic cancer is surgical removal of the tumors. However, for smaller tumors (max. 5 cm in diameter), hyperthermia treatment can be used. For pancreatic tumors, the most common treatment is radiofrequency ablation (RFA), which heats the tumor area using a high-frequency (on the order of hundreds of kHz) current. Unfortunately, current heating is not suitable for heating larger volumes of tissue, as only a small area around the catheter is actively heated by the current and more distant areas must be heated passively. Passive heating is complicated by blood vessels that dissipate heat and cool the area. [3] However, most of the RFA problem is solved by microwave ablation (MWA), which is a relatively new ablation method. Compared to RFA, MWA uses microwave waves most commonly in the frequency range of 900 MHz to 2450 MHz [4, 5]. This technique does not use an electric current to warm the tissue but employs an electromagnetic (EM) field which alters the spatial arrangement of water molecules, causing the tissue to heat up [5, 6].

2. METHODS

Due to the anatomical requirements of the pancreas, it was determined that the microwave catheter for ablation of pancreatic tumors should have a maximum diameter of 4.2 mm (12 Fr). The operating frequency of 2.45 GHz was chosen due to the availability of microwave

generators. For the catheter design, the Coaxial Cable U Low Loss Microwave Coax, 24 AWG from Temp-flex was selected. The microwave catheter was first simulated in the COMSOL multiphysics according to the datasheet for this coaxial cable.

3. RESULTS

Two versions of the microwave catheter were designed and simulated using COMSOL multiphysics. The first design comprised a simple catheter with one slot and a shorted end. The simulations revealed the optimal S11 parameter values (-21 dB) were achieved when the slot width was 6 mm at a distance of 2 mm from the catheter's distal end. The second simulated catheter featured a choke to dampen catheter back reflections, resulting in This catheter attained the minimum S11 parameter value of -23.5 dB.

Only one catheter slot was selected for the design, which was constructed according to the simulations performed. The slot was 6mm wide and located 2mm from the distal end. However, the catheter had a resonant frequency of 2.8GHz when measured on a vector analyser. Therefore, another catheter was constructed with a slot width of 1mm, situated 8mm from the distal end. This catheter is illustrated in Figure 1 and had a resonance frequency of 2.4GHz when measured.

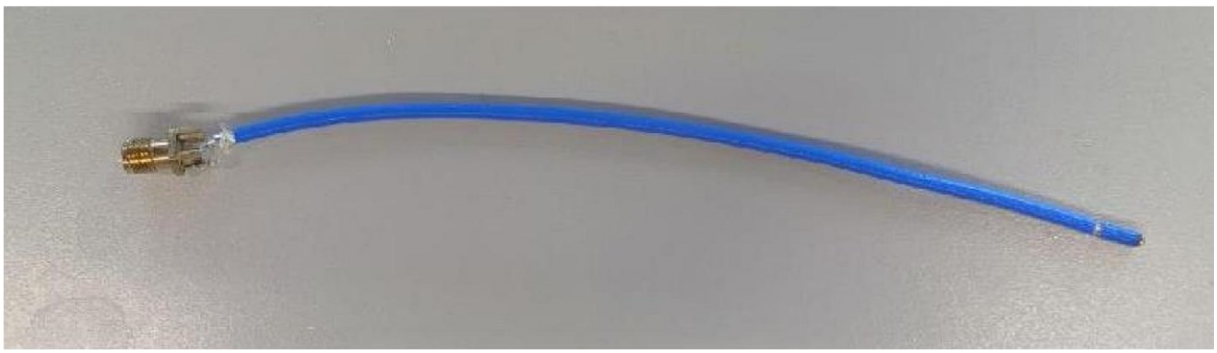

Figure 1: Final catheter

4. DISCUSSION

For the first catheter that was constructed, it was discovered that the resonant frequency did not correspond with the simulations. This could be a result of imprecision during the catheter's manufacture or could be because certain circumstances were not considered during the simulations. Additionally, the resonant frequency can also be influenced by the environment in which the catheter was measured. In this case, the parameters of the environment did not match the simulated parameters.

5. CONCLUSION

In this study, two models of microwave catheters were developed using COMSOL Multiphysics software. The first catheter featured a single slot, while the second catheter included a choke. Based on the simulations, a simple catheter was constructed whose resonant frequency did not match the simulated one. Therefore, a second catheter was constructed which already had a resonant frequency of 2.4 GHz.

REFERENCES

[1] AMERICAN SOCIETY OF CLINICAL ONCOLOGY (ASCO). Pancreatic Cancer: Statistics. Cancer.net [online]. 2021 [cit. 2023-06-24]. Dostupné z: https://www.cancer.net/cancertypes/pancreatic-cancer/statistics

[2] YADAV, Siddhartha, Prabin SHARMA a Dana ZAKALIK. Comparison of Demographics, Tumor Characteristics, and Survival Between Pancreatic Adenocarcinomas and Pancreatic Neuroendocrine Tumors. American Journal of Clinical Oncology [online]. 2018, 41(5), 485-491 [cit. 2023-04-17]. ISSN 0277-3732. Dostupné z: doi:10.1097/COC.0000000000000305

[3] AHMED, Muneeb, Christopher L. BRACE, Fred T. LEE a S. Nahum GOLDBERG. Principles of and Advances in Percutaneous Ablation. Radiology [online]. 2011, 258(2), 351-369 [cit. 2023-06-24]. ISSN 0033-8419. Dostupné z: doi:10.1148/radiol.10081634

[4] TAMMAM, Emad, Ashraf M. SAID, Ahmed A. IBRAHIM a Ahmed I. A. GALAL. About the Interstitial Microwave Cancer Ablation: Principles, Advantages and Challenges. IEEE Access [online]. 2020, 8, 49685-49694 [cit. 2021-03-22]. ISSN 2169-3536. Dostupné z: doi:10.1109/ACCESS.2020.2978210

[5] WOOD, Bradford J., Jochen KRUECKER, Nadine ABI-JAOUDEH et al. Navigation Systems for Ablation. Journal of Vascular and Interventional Radiology [online]. 2010, 21(8), 257-263 [cit. 2021-03-14]. ISSN 10510443. Dostupné z: doi:10.1016/j.jvir.2010.05.003

[6] HOFFMANN, R., H. REMPP a S. CLASEN. Mikrowellenablation. Der Radiologe [online]. 2012, 52(1), 22-28 [cit. 2023-06-24]. ISSN 0033-832X. Dostupné z: doi:10.1007/s00117-011-2208-9

USE OF UWB ANTENNA FOR HYPERTHERMIC TREATMENT OF GLIOBLASTOMAS

Fojtík Adam

Department of Biomedical Technology, Faculty of Biomedical Engineering,
Czech Technical University in Prague, Kladno, Czech Republic

ABSTRACT

This project deals with the optimization of a UWB antenna for hyperthermic treatment. The goal of that project was to achieve a suitable optimization of the antenna for the frequencies 434 and 2450 MHz, while the value of the reflection coefficient, for the said frequencies, should be below the value of -10 dB. This was achieved in the Sim4Life environment, where the original antenna was dimensionally modified using appropriate functions. These modifications were needed in order for the hyperthermic treatment to take place effectively. In terms of antenna dimensional adjustments, more specifically, bowtie arms of the antenna have been enlarged. At the same time, simulations of modified antennas were carried out in Sim4Life to see if they meet the mentioned conditions. After several adjustments, the optimal dimensions of the antenna were achieved with the results of reflection coefficients -11.45 dB for 434 MHz and -16.68 dB for 2450 MHz. The modified antenna was used in the next simulation, where it was equidistantly distributed around the tumor head model. Then field optimization took place using the optimizer software that uses a criterion function (wave stacking occurs here) which graphically displayed the resulting absorbed energy throughout the model. The results showed that the modified antenna could become a useful applicator in hyperthermic treatment.

1. INTRODUCTION

Unfortunately, tumors represent a high incidence and mortality rate. In our work, we specifically deal with brain tumors, more precisely glioblastoma. It is the most common and most malignant intracranial brain tumor. Based on recent studies, the occurrence of glioblastoma stands at 2 to 3 new cases per 100,000 individuals annually. With optimal treatment, patients live an average of 12 months and less than 10% survive 5 years. The incidence of new cases remains relatively consistent on a global scale. [1] For this reason, it is worthwhile to deal with the cancer treatment and thereby perhaps help patients.

2. METHODS

2.1 Modeling of the UWB antenna

Due to the fact that this project dealt only with modifying the model, there was no need to create new objects except for the block that was attached to the antenna and is supposed to simulate the patient's head. Furthermore, it was necessary to modify the existing model using the Move and Stretch functions. The final model looked like this, with a block added in front of the modified antenna to simulate brain tissue with dimensions of 150 × 200 × 150 mm.

2.2 UWB antenna simulation

The simulation involves the definition of materials, configuration of the source, selection of an appropriate grid, and subsequent discretization of the model voxels. For the clarity of the definition of materials, a table with the corresponding relative permittivity and electrical conductivity for specific materials is presented here (see in Table 2.1). The simulation calculation was performed by using the RUN function.

Table 2.1: Dielectric parameters of the materials used for a frequency of 3.5 GHz

	Relative permittivity (−)	Electrical conductivity (S/m)
Substrate	3.65	0.0004
Brain tissue	45.6	1.8
PEC	infinite	infinite
Air	1	0

2.3 Analysis

After performing the simulation calculation, the results were available in the analysis section. In our case $|S_{11}|$ parameters, which were subsequently exported in the form of CSV. We were also interested in the Specific absorption rate (SAR) in the tumor. In order to be able to measure SAR in the tumor, it was necessary to create a new multiport simulation and slightly modify the existing model. The modification consisted in the equidistant distribution of the modified antenna around the head model with the tumor in the middle.

2.4 Processing of results in MATLAB

First, we loaded the measured values from S4L into MATLAB, then we defined the variables, we converted the columns of values into homogeneous fields using the table2array function so that they could be made into a graph. After plotting the graph, it is verified whether the measured values met the project specification by achieving the condition $|S_{11}| < -10$ dB.

3. RESULTS

A comparison between the original antenna (left) and the modified (right) can be found in Figure 3.1

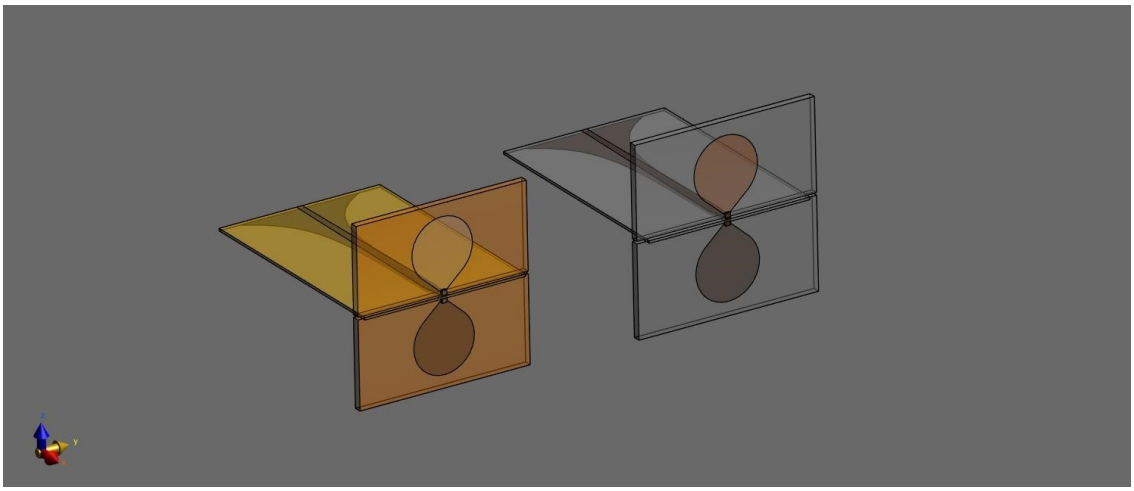

Figure 3.1: Comparison of original (36 × 36 mm) and modified (38 × 38 mm) UWB antenna

The obtained data exported from MATLAB contained the calculated values $|S_{11}|$ parameter depending on the frequency. The graph in Figure 3.2 was then created from them.

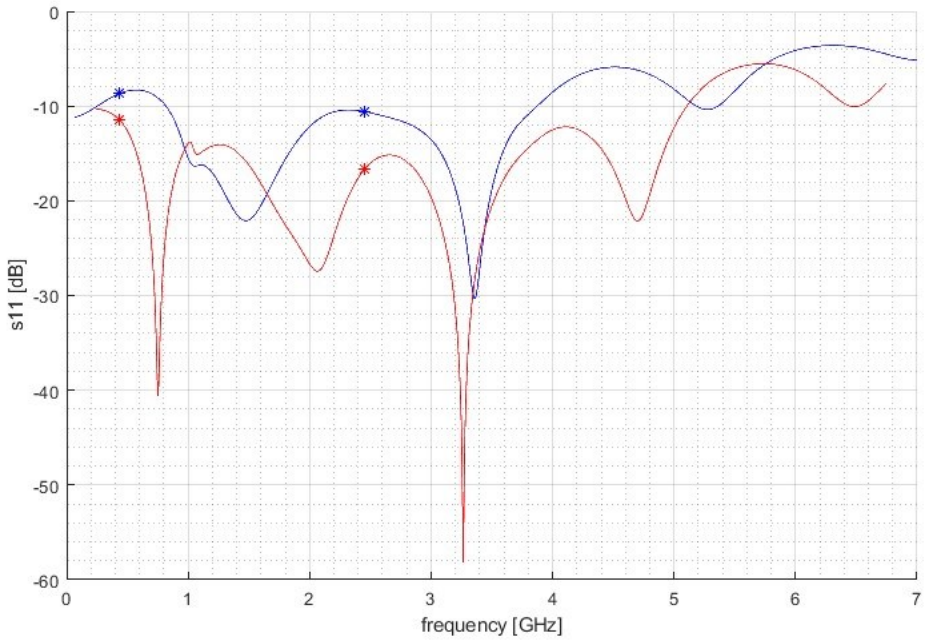

Figure 3.2: Visualization of $|S_{11}|$ parameter for the frequency band of the original (blue) and modified (red) antenna in MATLAB

Since we specifically dealt with hyperthermia, only the frequencies of 434 and 2450 MHz were essential for us. These frequencies were from the project brief and are based on previous studies and research. For this reason, it was enough for us to find out the values of $|S_{11}|$ for specific frequencies and then compare them with each other. The measured values are listed in Table 3.1.

Table 3.1: Values of $|S_{11}|$ parameter for specific frequencies

UWB antennas	$\|S_{11}\|$ (dB)	
	434 MHz	2450 MHz
Original	-8.68	-10.58
Modified	-11.45	-16.68

When the amplitudes and phases were optimized, there was energy absorption in the tumor observable as shades of red and pink in the middle of the model (see in Figure 3.3). This actually manifests itself as heating of the relevant tissue, which leads to a slowing down of cell division or to its complete destruction.

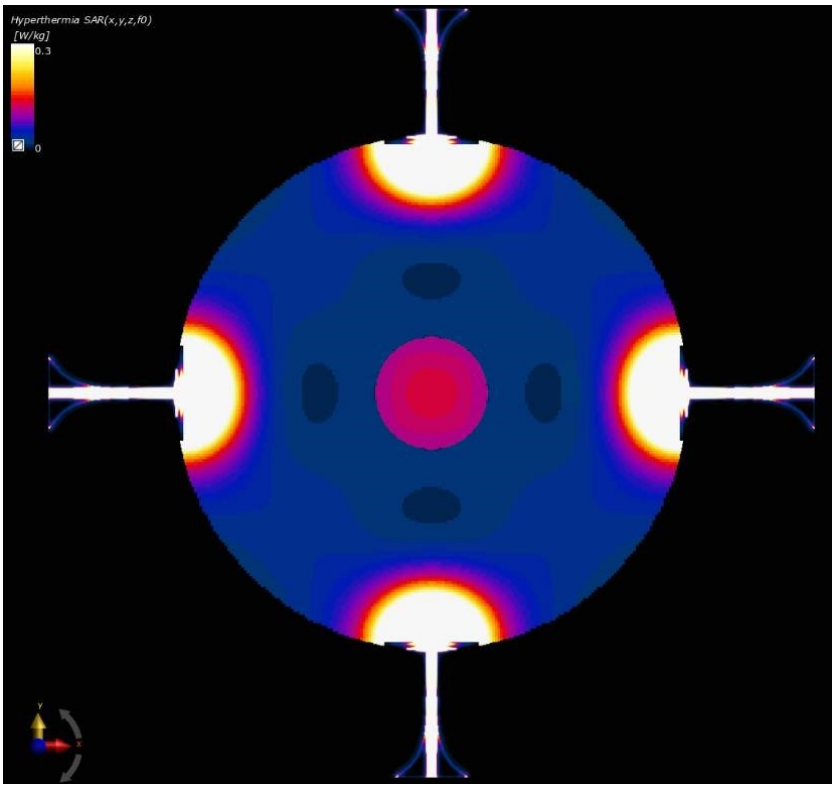

Figure 3.3: Optimized model to maximize SAR in the tumor

4. DISCUSSION

After many modifications of the antenna, it was possible to reach the point where the modified antenna showed the desired characteristics. The modification mainly consisted in enlarging the arms of the antenna. Since the shape of the arms is irregular and it was necessary to somehow map the change in size, a comparison using the area was chosen, where the arms of the original antenna had an area of 270.689 mm^2 and the area of the modified arms was 298.435 mm^2. Although there was a 10.25% increase, there was a sufficient change. Correct impedance matching has occurred with the modified antenna. We got the reflection coefficient below -10 dB, more specifically to -11.45 dB for the frequency of 434 MHz and to a value of -16.68 dB for the frequency of 2450 MHz, despite the original antenna was already optimized for the frequency of 2450 MHz, so the modification resulted in its improvement. The optimization of the amplitude and phase of the individual antenna elements went well. After equidistant distribution of modified antennas around the head with a tumor, optimization software operating on the principle of a criterion function was launched by the project supervisor. The optimization results are shown in Figure 2.3. The image shows that the power was absorbed by the tumor and minimally absorbed by the tumor's surroundings. Regarding the

results of the modified antenna, it is possible to state that the antenna was adjusted to the required parameters and with the help of which it was possible to heat even the tumor located in the middle of the head. Since no more rigorous and detailed antennas have been made so far, further improvement of antennas is inevitable. And since it is an alternative treatment in the phase of preclinical testing with beneficial results, as can be seen from some publications, this topic could become attractive for other people interested in the issue.

5. CONCLUSION

A proper optimization of the UWB antenna for hyperthermic treatment could become suitable and alternative to the current treatment of glioblastomas. Firstly, it is a non-invasive treatment and secondly enables almost immediate control of treatment effectiveness. Assignment and goals of this project, carrying out a study of the use of the UWB antenna, for hyperthermic treatment in a suitable of the EM field simulator (S4L), further its optimization so that it is impedance-matched ($|S_{11}| < -10$ dB) at frequencies 434 and 2450 MHz, were met. The antennas were also modified equidistantly spaced around the tumor head model where using the available software has optimized amplitudes and phases to maximize absorbed energy in the tumor.

6. ACKNOWLEDGMENT

I would like to thank doc. Ing. Ondřej Fišer, Ph.D. to my Semester Project 1 supervisor for helping me with the Sim4Life environment, for valuable and constructive advice. I would also like to thank Ing. Jan Rédr for valuable advice.

REFERENCES

[1] WikiSkripta. Glioblastoma multiforme, 2018 [Online]. Available: https://www.wikiskripta.eu/w/Glioblastoma_multiforme. [cit. 2023-03-18].

Effect of calibration standard selection on the accuracy of biological tissue dielectric measurements

Zdenek Linha

Department of Biomedical Technology, Faculty of Biomedical Engineering,
Czech Technical University in Prague, Kladno, Czech Republic

Abstract: The measurement of dielectric parameters of biological tissues using the open-ended coaxial probe is one of the most widely used due to its non-invasiveness and non-destructiveness to the measured sample. However, commercial systems are expensive and a affordable alternative would allow more research groups to contribute to the development of new methods based on electromagnetic field. The objective of this work was to select a combination of calibration standards providing the most accurate dielectric parameter values using an affordable vector network analyzer (VNA) and coaxial probe.

The reflection coefficients were converted by an antenna model of the coaxial probe with calibration using three calibration standards. The measured dielectric parameters were filtered and fitted to a one-pole Cole-Cole model. The calibration standards considered included SHORT, air (OPEN), deionized water (DI), isopropanol (IPA), ethanol (ETH), dimethyl sulfoxide (DMSO), ethylene glycol (EG) and methanol (MET). PocketVNA, Germany, and a coaxial probe with an outer diameter of 2.2 mm, Rohde&Schwarz, Vimperk, Czech Republic, were used for the measurements. The selected frequency band was from 70 MHz to 3 GHz. Three biological tissues were measured: muscle, liver and adipose. The reference was the measurement with VNA N9923 FieldFox, Keysight Technologies, USA and coaxial probe DAK 12, SPEAG, Switzerland.

Based on the measured data, most promising results were achieved using the combination of DI, OPEN and either DMSO or EG. In the summary the accuracy of measurement with different calibration standards was presented using an affordable VNA and coaxial probe. In future works the accuracy of a wider probe will be evaluated to negate the effect of sensing volume.

Guiding the selection of the optimal transseptal puncture site during catheter insertion for left atrial appendage closure using phantoms of the left and right atria

Michaela Široká

Department of Biomedical Technology, Faculty of Biomedical Engineering,
Czech Technical University in Prague, Kladno, Czech Republic

1. INTRODUCTION

Atrial fibrillation is the most common type of sustained cardiac arrhythmia, increasing the risk of ischaemic stroke by four to five times and is the main cause of nearly 20 % of all strokes. Echocardiography and autopsy studies show that up to 90 % of left atrial thrombi are localized in the left atrial appendage (LAA), from where they travel through the left ventricle most often directly to the brain when released [1, 2]. In cases, where standard treatment, i.e. oral anticoagulation therapy, is contraindicated or not effective, a non-pharmacological option may be left atrial appendage closure (LAAC) [3]. LAAC is a technically challenging transcatheter-based procedure. Therefore, preprocedural planning is crucial to reduce the risk of severe complications. The choice of transseptal puncture site is one of the most important factors in this regard [3, 4, 5]. LAAC device manufacturing guidelines routinely suggest a transseptal puncture in the postero-inferior quadrant [6]. However, preprocedural planning using 3D printed models suggested that in approximately half the patients an alternative quadrant would be the optimal puncture site [6].

AIMS OF THE STUDY

The aim of the study is to create numerical and 3D printed anatomical models of the left and right atria from anonymized patient CT images in a segmentation program, i.e. to differentiate all inlet and outlet openings, and to create catheter insertion holes in the area of the foramen ovale. The next goal is to print these models using the 3D printing method.

2. METHODS

The initial data were anonymized cardiac CT scans of patients who underwent left atrial appendage closure and also had a known ideal site for transseptal septal puncture. Numerical models of the left and right atria were created from the data by segmentation in the 3D slicer software - semi-automatic segmentation function was used followed by manual adjustment. In the area of the foramen ovale, 6 holes for catheter insertion were created in Sim4Life light

software. The models were printed on a Prusa MK3S+ 3D printer using Prusament PETG filament.

3. RESULTS

The printed model of the left and right atrium is shown in Figure 1. All inlet and outlet openings are described in the figure.

(a) (b)

Figure 1. Printed model of the left and right atria: (a) back view, (b) front view

4. DISCUSSION

The initial data were anonymized images from cardiac CT scans. The semi-automatic segmentation method was used in 3D slicer to segment them, but it proved to be inappropriate in cases where the quality of CT images is reduced, e.g. by artifacts caused by the presence of a pacemaker. Therefore, such data have not been used at this stage of the work yet, as they would need additional adjustments before segmentation.

5. CONCLUSION

In this study, 3 anatomical numerical models of the right and left atria were created by segmenting CT images, differentiating all inlet and outlet openings - i.e. the superior and inferior vena cava, pulmonary arteries and inlets to both ventricles. The models were subsequently printed by 3D printing.

ACKNOWLEDGMENT

The results will be used in a follow-up study to develop a methodology for automated determination of the ideal site for transseptal puncture during left atrial appendage closure, which is a key factor for the successful performance of this procedure.

REFERENCES

[1] BLACKSHEAR, Joseph L. a John A. ODELL. Appendage obliteration to reduce stroke in cardiac surgical patients with atrial fibrillation. The Annals of Thoracic Surgery. 1996, 61(2), 755-759. ISSN 00034975. Available from: doi:10.1016/0003-4975(95)00887-X

[2] LEVENTIĆ, Hrvoje, Danilo BABIN, Lazar VELICKI, Daniel DEVOS, Irena GALIĆ, Vladimir ZLOKOLICA, Krešimir ROMIĆ a Aleksandra PIŽURICA. Left atrial appendage segmentation from 3D CCTA images for occluder placement procedure. Computers in Biology and Medicine. 2019, 104, 163-174. ISSN 00104825. Available from: doi:10.1016/j.compbiomed.2018.11.006

[3] PELLEGRINO, PIER LUIGI, GAETANO FASSINI, MATTEO DI BIASE, CLAUDIO TONDO, Horst SIEVERT, Shephal K. DOSHI, Kenneth HUBER a Vivek Y. REDDY. Left Atrial Appendage Closure Guided by 3D Printed Cardiac Reconstruction: Emerging Directions and Future Trends. Journal of Cardiovascular Electrophysiology. 2016, 27(6), 768-771. ISSN 10453873. Available from: doi:10.1111/jce.12960

[4] WANG, Dee Dee, Marvin ENG, Daniel KUPSKY, et al. Application of 3-Dimensional Computed Tomographic Image Guidance to WATCHMAN Implantation and Impact on Early Operator Learning Curve. JACC: Cardiovascular Interventions. 2016, 9(22), 23292340. ISSN 19368798. Available from: doi:10.1016/j.jcin.2016.07.038

[5] HUMPHRIES, Julie A. The Use of Transesophageal Echocardiography to Guide Percutaneous LAA Closure. Left Atrial Appendage Closure. Cham: Springer International Publishing, 2016, 2016, 83-100. Contemporary Cardiology. ISBN 978-3-319-16279-9. Available from: doi:10.1007/978-3-319-16280-5_6

[6] CIOBOTARU, Vlad, Nicolas COMBES, Claire A. MARTIN, et al. Left atrial appendage occlusion simulation based on three-dimensional printing: new insights into outcome and technique. EuroIntervention. 2018, 14(2), 176-184. ISSN 1774-024X. Available from: doi:10.4244/EIJ-D-17-00970

The influence of regional hyperthermia applicators on the B1+ field homogeneity of the MRI system

Michael Vydra

Department of Biomedical Technology, Faculty of Biomedical Engineering,
Czech Technical University in Prague, Kladno, Czech Republic

Abstract—The homogeneity of the B_1^+ field is an important factor for correct magnetic resonance imaging. The aim of this work was to determine the effect of two hyperthermia (HT) applicators on the homogeneity of the B_1^+ field and to calculate the temperature rise caused by radiofrequency (RF) exposure of the MRI system during non-invasive temperature measurements. Using an electromagnetic field simulator, an RF birdcage coil was modelled and tuned to a resonant frequency of 64 MHz. Two HT applicators and three 3D patient models were placed inside the birdcage coil. The effect of different parts of the HT applicator on the B_1^+ field was determined. The water filling of the HT applicator has the largest effect on the field change and the maximum value of the field increases for Sigma-Eye applicator from 6.00 μT up 32.97 μT with a variance of ± 8.72 μT within a radius of 20 cm from the centre of the coil. The maximum values of the temperature increase caused by RF exposure correspond to those caused by conventional scanning. The predicted B_1^+ field values are comparable to the measured ones.

1. INTRODUCTION

One of the main components of magnetic resonance imaging (MRI) are radio frequency (RF) coils which transmit and receive signals. RF coils generate a RF field B_1 perpendicular to the main magnetic field B_0 which can be divided into two components: The component that rotates in the same direction as the nuclear precession (B_1^+) and the component that rotates in the opposite direction (B_1^-). Only the B_1^+ sub-field is responsible for the reversal of the nuclear magnetization. Nowadays almost all RF coils are circularly polarized, which (ideally) eliminates the effects of the B_1^- subfield, i.e.: $B_1^+ = B_1$ and $B_1^- = 0$. [1,2,3] Radiofrequency coils, known as birdcage coils, are widely used in MRI. Birdcage coils can produce a very homogeneous magnetic field in the desired volume with a high signal-tonoise ratio (SNR). [4,5]

During magnetic resonance imaging, the human body is exposed to the RF pulses required for imaging, which are absorbed by the body and converted to heat. The best way to describe

the electromagnetic energy absorbed by biological tissue is the Specific Absorption Rate (SAR). [6,7] Clinical trials have shown that hyperthermia (HT), i.e., an increase in tissue temperature to 40-44 °C, significantly increases the efficiency of radiotherapy and chemotherapy [8]. Regional HT uses constructive interference, where individual electromagnetic (EM) fields interfere to form a single SAR distribution, which is then converted into a temperature map. [9, 10, 11] It has been known for over 30 years that MRI can be used to non-invasively measure temperature and its changes in the human body. In MRI, temperature is measured in space using 3D MR thermometry methods. The most used method, proton resonance frequency (PRF) MR thermometry which is the result of a phenomenon called chemical shift. [12,13,14]

The inhomogeneity of the B_1^+ field can lead to a reduction in image intensity and the formation of artefacts. By improving the homogeneity of the B_1^+ field, it is possible to improve the quality of the subsequent image uniformity, increase the SNR factor and possibly reduce the SAR. Temperature monitoring is important in hyperthermia treatment. Magnetic resonance thermometry is a method that provides non-invasive 3D spatial temperature monitoring.

2. METHODS

In the Sim4Life electromagnetic field simulator, a birdcage model of the 1.5T MRI high-pass coil was created, see the schematic in Figure 1(a). The coil was tuned to have a resonant frequency of 64 MHz, i.e. the Larmor frequency for 1.5T MRI. Finite-difference time-domain method (FDTD) was used to calculate the electromagnetic field of an empty coil to set the basis for the evaluation of the homogeneity change. [15] To determine the effect of hyperthermia applicators, models of two different applicators were used, see Figure 1 (b) and (c). The Sigma-Eye applicator used for treatment in the pelvic region and the Hyper-Collar applicator used for treatment in the head region.

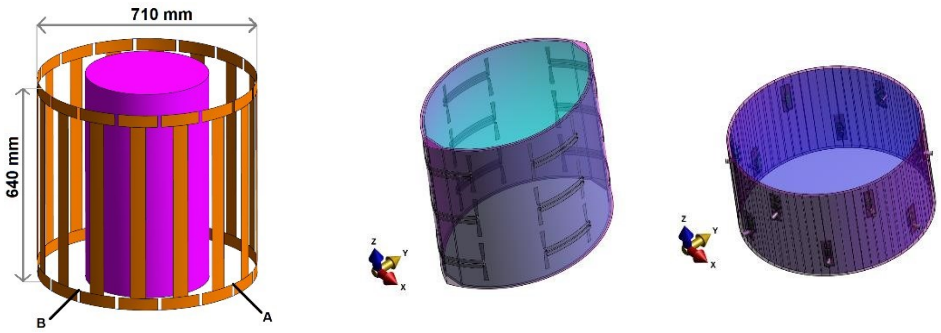

(a) Birdcage (b) Sigma-Eye (c) Hyper-Collar

Figure 1. Models of (a) Birdcage coil, (b) Sigma-Eye applicator, (c) Hyper-Collar applicator

To obtain the most realistic results, three different 3D patient models were used. The first model was created by segmenting CT scans, where CT scans in the form of DICOM files were taken from the available database of The Visible Human Project. The segmentation result can be seen in Figure 2 (a). The other two models were obtained from the Sim4Life Virtual Population database. These are the Duke model and the Ella model see Figure 2 (b) and (c).

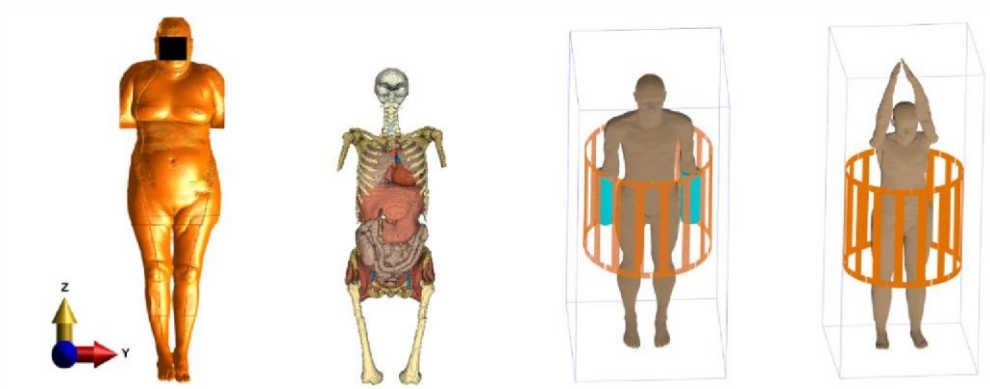

(a) CT (b) Duke (b) Ella

Figure 2. Display of 3D patient models. (a) Model created by segmentation of CT scans and the display of its internal tissue segmentation, (b) model Duke, (c) model Ella

When using HT applicators for the pelvic area, the patient in the MRI is required to raise their arms to target the desired area. The available patient model, Duke V3.0, does not allow the hands to be raised, therefore the patient's hands were placed in cylinders with local environment material properties. A complete list of all the tissues used is available on the website of the Foundation for Research on Information Technologies in Society (IT'IS), from which they were taken. [16,17] Since there was a slowdown in the calculation of the temperature simulations due to certain tissue parameters resembling air in density, the specific heat capacity of these tissues has been increased by a factor of 10 see table 1. [10]

Table 1. List the patient model tissues for which some of their physical parameters were modified.

Tissue	**Density** ρ (kg/m^3)	**Specific heat capacity** c (J/kg/K)	**Thermal conductivity** λ (W/m/K)
Bronchial filling	1,164	10037†	0,027
Esophageal filling	1,164	10037†	0,027
Inner air	1,164	10037†	0,027
Trachea filling	1,000	10040†	0,030

† The specific heat capacity has been increased by a factor of 10 to speed up the thermal calculations, which has no effect on the temperature change. This theoretical note was taken from a study [10].

To investigate the temperature increase due to RF MRI exposure, a 90-minute HT treatment simulation was created to warm the patient up to 44°C, to which RF exposure was added. The treatment was not specifically targeted. The RF scan was switched on in 10-minute scan sequences for a time limited by the selected 10% duty-cycle. The heat generated is distributed throughout the simulated area by thermal diffusion and is calculated using Penne's Bioheat Equation:

$$\rho c \frac{\partial T}{\partial t} = \nabla \cdot (k \nabla T) + \rho Q + \rho S - \rho_b c_b \rho \omega (T - T_b) \quad (1)$$

where the expression $\rho_b c_b \rho \omega$ is referred to as the heat transfer rate and acts as both heating and cooling as it represents the flow of blood.

3. RESULTS

Here are the results that were processed in the software MATLAB. An empty birdcage coil, tuned to a resonant frequency, provides an internally very homogeneous B_1^+ field of (6.00 ± 0.03) μT within a radius of 20 cm from the centre, see Figure 3 (a) (the values are written in the form of absolute value and variance: $|B_1^+| \pm \sigma$). If this field is cut, as shown by the green line in Figure 3 (a), a 2D plot of the B_1^+ field is obtained, see Figure 3 (b).

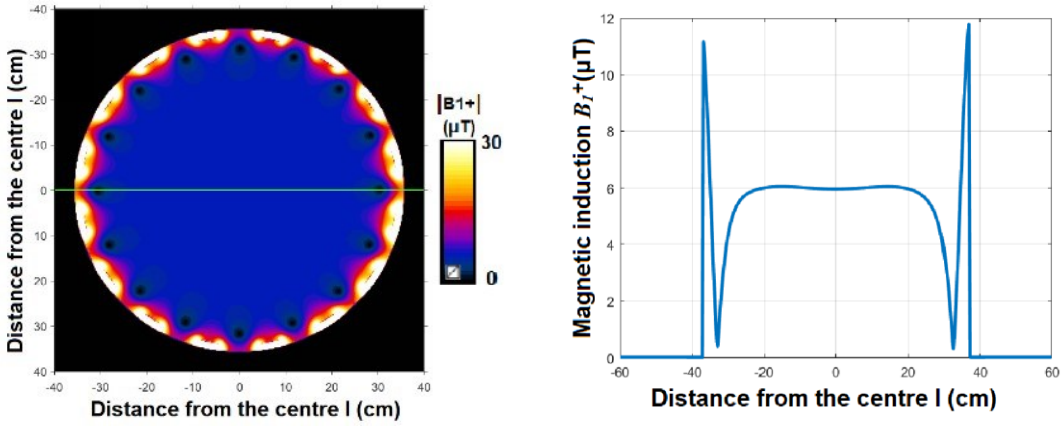

(a) B_1+ field (b) B_1^+ field in slice

Figure 3. Homogeneous B_1^+ field of an empty tuned coil, (a) B_1^+ field where the green line shows the location of the slice, (b) B_1^+ field in slice.

The B1 field value changes due to the Sigma-Eye applicator to (28,51 ± 8,72) μT and due to the Hyper-Collar applicator to (7,29 ± 0,91) μT. The changes are evident in Figure 4. Simulations without applicator antenna elements do not change these results.

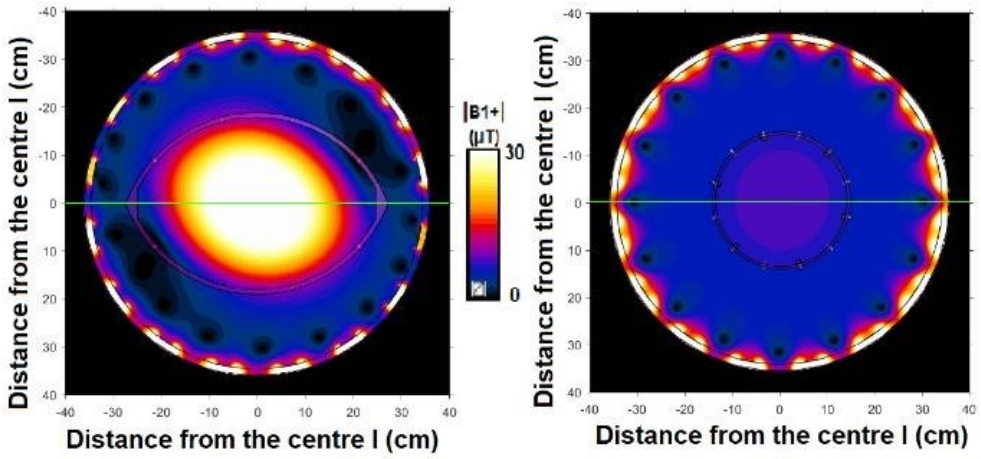

(a) Sigma-Eye (b) Hyper-Collar

Figure 4. Change in field homogeneity due to HT applicator, (a) B_1^+ field with model of Sigma-Eye applicator, (b) B_1^+ field with model of Hyper-Collar applicator,

Figure 5 (a) and (b) shows the result of simulated hyperthermia treatment and RF-MRI exposure, where the maximum difference in median temperature is 0.03°C (ΔT = (med. $THT{+}RF$ − med. THT)). A comparison of the simulation results with the measured values from Erasmus MC Rotterdam is shown in Figure 5 (c) and (d).

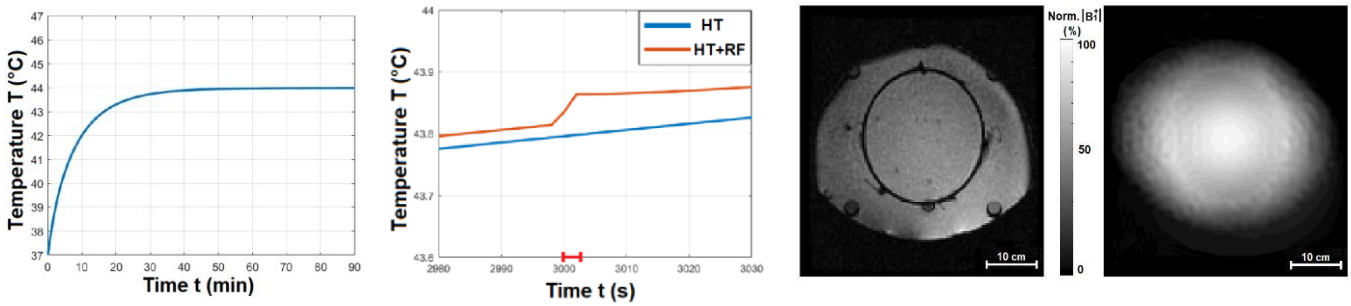

(a) HT treatment (b) RF exposition (c) Erasmus MC (d) Simulation

Figure 5. First two figures show the results of temperature simulations to determine the heating due to RF MRI exposure. Figure (c) and (d) show a comparison of the simulation results against measured data from Erasmus MC.

4. DISCUSSION

According to the simulations, the water bolus of the HT applicator itself has the greatest influence on the homogeneity of the B_1^+ field. As a factor affecting the homogeneity of the B_1^+ field, a variance of values was chosen where the field varying by more than 1.00 μT within a radius of 20 cm from the centre of the coil, i.e. ± 0.5 μT, could affect the quality of MR imaging. The reference empty coil produced a homogeneous field of (6.00 ± 0.03) μT. The RF field is removed using the RF shield, and therefore the value of the B_1^+ field in the space behind the RF

shield of the birdcage cell is zero. This is at the cost of a large increase in the B_1^+ field closer to the inner part of the RF shield.

The homogeneity of the B_1^+ field depends on the size of the object placed in the coil and its material properties. Firstly, simulations of HT applicators without PEC antennas were carried out to determine the effect of the water bolus itself filling the HT applicator. These results indicate that the antenna elements of the HT applicators may cause a local B_1^+ field peak but do not have a significant effect on the overall homogeneity. The SAR increases in proportion to the increase in the B_1^+ field. The comparison was made with data from Erasmus MC, Rotterdam. During the simulation, the same B_1^+ field is observed in the water column region of the Sigma-Eye applicator as in the measurements. As the phantom was not centred during the measurement, the B_1^+ field is not symmetrical in the direction from the centre of the coil. The limiting factor is the fact that the objects placed in the birdcage coil itself have certain capacitive properties and therefore a slight shift in the resonant frequency of the coil may occur.

5. CONCLUSION

In this study, the effects of two hyperthermia applicators on the predicted B_1^+ field homogeneity were determined by simulations. The water bolus of the HT applicators alone has the greatest effect on the B_1^+ field homogeneity. The largest change in homogeneity occurs with the Sigma-Eye HT applicator, where the variance of values increased from ± 0.03 μT to ± 8.72 μT within a radius of 20 cm from the centre of the coil. The maximum values of the temperature rise caused by RF exposure of the MRI system correspond to those caused by conventional MRI scanning. The predicted B_1^+ field values are comparable to the measured ones. The results of this work can serve as a contribution to the development of better hyperthermia treatment planning in combined MRI HT systems.

ACKNOWLEDGMENT

I would like to thank my supervisor, Ing. Tomáš Dřížďal, Ph.D., for his professional guidance, valuable advice, and consultation that he provided during the preparation of my thesis. I would like to thank Erasmus MC, Rotterdam, for providing the data from the B_1^+ field measurements.

REFERENCES

[1] ANDERSON, Cynthia et al. *The Role of MRI in Radiation Therapy Planning.* USA: Siemens Medical Solutions, 2011.

[2] ELSTER D., Allen et al. *Questions and Answers in MRI*. Mallinckrodt Institute of Radiology, 2022. ⟨www.mriquestions.com⟩.

[3] HAYES E., Celis et al. *An efficient, highly homogeneous radiofrequency coil for whole-body NMR imaging at 1.5 T.* Journal of Magnetic Resonance. Vol. 63, 1985

[1] GIOVANNETTI, Giulio et al. *A fast and accurate simulator for the design of birdcage coils in MRI.* Magma (New York, N.Y.), Vol 15, p. 36–44, 2002

[2] WANG, Jinghua et al. *Factors influencing flip angle mapping in MRI: RF pulse shape, slice-select gradients, off-resonance excitation, and B_0 inhomogeneities.* Magnetic Resonance in Medicine. Vol. 56, No. 2, p. 463–468, 2006

[3] VRBA, Jan. *Lékařské aplikace mikrovlnné techniky*. CTU, Prague, 2003.

[4] MURBACH, Manuel et al. *Thermal tissue damage model analysed for different whole-body SAR and scan durations for standard MR body coils.* Magnetic resonance in medicine. Vol. 71, No. 1, p. 421–431, 2014

[5] VAN DER ZEE, Jill. *Heating the patient: a promising approach?* Annals of oncology. Vol. 13, No. 8, p. 1173–1184, 2002

[6] GELLERMANN, Johanna et al. *Simulation of different applicator positions for treatment of a presacral tumour.* International Journal of Hyperthermia. Vol. 23, No. 1, p. 37–47, 2007

[7] MARGARETHUS, M. Paulides et al. *ESHO benchmarks for computational modeling and optimization in hyperthermia therapy.* International Journal of Hyperthermia. Vol. 38, No. 1, p. 1425–
1442, 2021

[8] KOK, H. Petra; CREZEE, J. *Validation and practical use of Plan2Heat hyperthermia treatment planning for capacitive heating*. International Journal of Hyperthermia. Vol. 39, No. 1, p. 952–966, 2022

[9] DRIZDAL, Tomas et al. *Influence of Deep-Region RF Hyperthermia System on B1+ Field of 1.5 T MR Scanner: a Simulation Study.* 2014

[10] BLACKWELL, James et al. *Proton resonance frequency shift thermometry: a review of modern clinical practices.* Journal of Magnetic Resonance Imaging., Vol. 55, No. 2, p. 389 - 403, 2022 [14] ODÉEN, Henrik; PARKER, Dennis L. *Magnetic resonance thermometry and its biological applications–Physical principles and practical considerations*. Progress in nuclear magnetic resonance spectroscopy. Vol. 110, No. 34–61, 2019

[15] CHI, Jieru a kol. *GPU-Accelerated FDTD Modeling of Radio-Frequency Field–Tissue Interactions in High-Field MRI*. IEEE Transactions on Biomedical Engineering. Vol. 58, No. 6, p. 1789–1796, 2011

[16] CHRIST, Andreas et al. *The Virtual Family—development of surface-based anatomical models of two adults and two children for dosimetric simulations*. Physics in Medicine and Biology. Vol. 55, No. 2, p. 23–38, 2009

[17] GOSSELIN, Marie-Christine et al. *Development of a new generation of highresolution anatomical models for medical device evaluation: the Virtual Population 3.0.* Physics in Medicine and Biology. Vol. 59, No. 18, p. 5287–5303, 2014

Design of power and control part for multichannel DDS generator

Daniel Ulbrich

Department of Biomedical Technology, Faculty of Biomedical Engineering,
Czech Technical University in Prague, Kladno, Czech Republic

Introduction: The hyperthermia system consists of several devices - a radio frequency generator, a temperature measurement set, a water pump, applicators, a water bolloon and a software [1]. Electromagnetic (EM) heating techniques use a sinusoidal alternating high frequency EM field generated by one or more antennas [2]. Direct digital synthesis (DDS) is a method of signal generation using digital, digital-to-analog or analog circuits. The analog output signal is obtained by generating a time-varying signal in digital form and then converting it to an analog signal [3].

Aims: The aim of work is to design the power supply and control part for a multichannel generator based on the integrated circuit AD9959 (Analog Devices), which uses DDS methods. The generator will be powered from the USB bus (5 V, 2 A) assuming operation of four AD9959 circuits simultaneously. Another aim of the work is to design a control part based on a microcontroller PIC18F (Microchip) that communicates with the computer via a USB bus.

Methods: The AD9959 contains four DDS circuits with a 10-bit DAC. The component is used to generate small signals with variable phase and amplitude. A microcontroller PIC18LF25K83 is used for communication between the PC and the circuit to generate RF signals. The whole generator circuit is powered from the USB connector (5 V). LM1117 voltage regulators are used to achieve lower supply voltages (1.8 V, 3.3 V) and MEMS oscillator for 50 MHz frequency is used in the clock frequency generation part.

Results: The four-layer PCB of the control and power supply part was done in EAGLE. The top and bottom layers are used for signal transmission and the remaining two layers for ground (GND) and power supply lines (5 V, 1.8 V, 3.3 V).

Conclusion and Discussion: The multichannel generator is based on the DDS principle. The function of this principle is represented in the circuit by the AD9959, which contains four DDS circuits. All outputs have independently adjustable phase and amplitude. USB power supply was chosen for the whole circuit. The lower supply voltages were necessary to power

the other components. It was 1.8 V and 3.3 V. The linear regulators LM1117 were used for this task. Communication between the PC and the circuit is provided by the microcontroller PIC18LF25K83.

The follow-up work leading to the completion of the multi-channel DDS generator consists in the design of the control part (interconnection of the microcontroller with the DDS circuits), filtering of the output signals for the 434 MHz frequency, programming the microcontroller in MPLAB and creating all the PCBs and the generator housing. Furthermore, the creation of a user interface of the multi-channel generator for setting the number of active channels, amplitudes and phases of each channels.

REFERENCES

[1] VRBA, Jan. *Lékařské aplikace mikrovlnné techniky*. Praha: Vydavatelství ČVUT, 2003. ISBN 80-010-2705-8.

[2] FOSTER, K. a H. SCHWAN. Dielectric properties of tissues and biological materials: A critical review. *Critical Reviews in Biomedical Engineering*. 1989, **17**(1), 25-104.

[3] MURPHY, Eva a Colm SLATTERY. All About Direct Digital Synthesis. *Analog Dialogue: Ask The Application Engineer* [online]. 2004, **38**(33) [cit. 2023-06-22]. Dostupné z: https://www.analog.com/en/analog-dialogue/articles/all-about-direct-digital-synthesis.html#author